Whole Earth Telescope observations of the hot helium atmosphere pulsating white dwarf EC20058-5234

D. J. Sullivan, T. S. Metcalfe, D. O'Donoghue, D. E. Winget, D. Kilkenny, F. van Wyk, A. Kanaan, S. O. Kepler, A. Nitta, S. D. Kawaler, et al.

▶ **To cite this version:**

D. J. Sullivan, T. S. Metcalfe, D. O'Donoghue, D. E. Winget, D. Kilkenny, et al.. Whole Earth Telescope observations of the hot helium atmosphere pulsating white dwarf EC20058-5234. Monthly Notices of the Royal Astronomical Society, 2008, 387, pp.137-152. 10.1111/J.1365-2966.2008.13074.X . hal-00287849

HAL Id: hal-00287849
https://hal.science/hal-00287849

Submitted on 15 Dec 2020

HAL is a multi-disciplinary open access archive for the deposit and dissemination of scientific research documents, whether they are published or not. The documents may come from teaching and research institutions in France or abroad, or from public or private research centers.

L'archive ouverte pluridisciplinaire **HAL**, est destinée au dépôt et à la diffusion de documents scientifiques de niveau recherche, publiés ou non, émanant des établissements d'enseignement et de recherche français ou étrangers, des laboratoires publics ou privés.

Mon. Not. R. Astron. Soc. **387,** 137–152 (2008) doi:10.1111/j.1365-2966.2008.13074.x

Whole Earth Telescope observations of the hot helium atmosphere pulsating white dwarf EC 20058−5234

D. J. Sullivan,[1⋆†] T. S. Metcalfe,[2,3] D. O'Donoghue,[4] D. E. Winget,[2] D. Kilkenny,[4,5] F. van Wyk,[4] A. Kanaan,[6] S. O. Kepler,[7] A. Nitta,[2,8,9] S. D. Kawaler[10] M. H. Montgomery,[2] R. E. Nather,[2] M. S. O'Brien,[10,11] A. Bischoff-Kim,[2] M. Wood,[12] X. J. Jiang,[13] E. M. Leibowitz,[14] P. Ibbetson,[14] S. Zola,[15,16] J. Krzesinski,[16] G. Pajdosz,[16] G. Vauclair,[17] N. Dolez[17] and M. Chevreton[18]

[1]*School of Chemical & Physical Sciences, Victoria University of Wellington, PO Box 600, Wellington, New Zealand*
[2]*Department of Astronomy and McDonald Observatory, University of Texas, Austin, TX 78712, USA*
[3]*High Altitude Observatory, National Center for Atmospheric Research, PO Box 3000, Boulder, CO 80307, USA*
[4]*South African Astronomical Observatory, PO Box 9, Observatory 7935, South Africa*
[5]*Department of Physics, University of the Western Cape, Private Bag X17, Belville 7535, South Africa*
[6]*Departamento de Física, UFSC, CP 476, 88040-900 Florianóplois, SC, Brazil*
[7]*Instituto de Física da UFRGS, 91501-900 Porto Alegre, RS, Brazil*
[8]*Visiting Astronomer, Cerro Tololo Inter-American Observatory, Chile*
[9]*Gemini Observatory, 670 N A'ohoku Pl., Hilo, HI 96720, USA*
[10]*Department of Physics & Astronomy, Iowa State University, Ames, IA 50011, USA*
[11]*Department of Astronomy, Yale University, PO Box 208101, New Haven, CT 06511, USA*
[12]*Department of Physics and Space Sciences and SARA Observatory, Florida Institute of Technology, Melbourne, FL 32901-6975, USA*
[13]*Beijing Astronomical Observatory, Chinese Academy of Sciences, 20 Datun Road, Chaoyang, Beijing 100012, China*
[14]*Department of Physics and Astronomy and Wise Observatory, Tel Aviv University, Tel Aviv 69978, Israel*
[15]*Astronomical Observatory, Jagiellonian University, Ul. Orla 171, 30-244 Cracow, Poland*
[16]*Mount Suhora Observatory, Pedagogical University, Ul. Podchoraazych 2, 30-024 Cracow, Poland*
[17]*Observatoire Midi-Pyrénées, Université Paul Sabatier, CNRS/UMR5572, 14 Avenue Edouard Belin, 31400 Toulouse, France*
[18]*Observatoire de Paris-Meudon, LESIA, 92195 Meudon, France*

Accepted 2008 February 5. Received 2008 February 5; in original form 2007 November 7

ABSTRACT

We present the analysis of a total of 177 h of high-quality optical time-series photometry of the helium atmosphere pulsating white dwarf (DBV) EC 20058−5234. The bulk of the observations (135 h) were obtained during a WET campaign (XCOV15) in 1997 July that featured coordinated observing from four southern observatory sites over an 8-d period. The remaining data (42 h) were obtained in 2004 June at Mt John Observatory in NZ over a one-week observing period. This work significantly extends the discovery observations of this low-amplitude (few per cent) pulsator by increasing the number of detected frequencies from 8 to 18, and employs a simulation procedure to confirm the reality of these frequencies to a high level of significance (1 in 1000). The nature of the observed pulsation spectrum precludes identification of unique pulsation mode properties using any clearly discernable trends. However, we have used a global modelling procedure employing genetic algorithm techniques to identify the n, ℓ values of eight pulsation modes, and thereby obtain asteroseismic measurements of several model parameters, including the stellar mass (0.55 $M_{\odot}$) and $T_{\rm eff}$ ($\sim$28 200 K). These values are consistent with those derived from published spectral fitting: $T_{\rm eff} \sim 28\,400$ K and $\log g \sim 7.86$. We also present persuasive evidence from apparent rotational mode splitting for two of the modes that indicates this compact object is a relatively rapid rotator with a period of 2 h. In direct analogy with the corresponding properties of the hydrogen (DAV) atmosphere pulsators, the stable low-amplitude pulsation behaviour of EC 20058 is entirely consistent with its inferred effective

⋆E-mail: denis.sullivan@vuw.ac.nz
†Visiting astronomer, Mt John University Observatory, operated by the Department of Physics & Astronomy, University of Canterbury.

© 2008 The Authors. Journal compilation © 2008 RAS

Downloaded from https://academic.oup.com/mnras/article/387/1/137/998283 by guest on 15 December 2020

temperature, which indicates it is close to the blue edge of the DBV instability strip. Arguably, our most significant result from this work is the clear demonstration that EC 20058 is a very stable pulsator with several dominant pulsation modes that can be monitored for their long-term stability.

Key words: techniques: photometric – stars: individual: EC 20058-5234 – stars: interiors – stars: oscillations – white dwarfs.

1 INTRODUCTION

Nearly 99 per cent of all stars are predicted to end their lives as slowly cooling white dwarfs; their study, among other things, provides an important perspective on the active lives of all the progenitor objects. In particular, if we can determine their internal chemical compositions, we have access to key data concerning the products of the nuclear reactions that power stars in the previous evolutionary stages. In common with other astronomical objects, we are largely limited to studying the atmospheres of white dwarfs as this is where the photons we detect are created. Thus, detailed spectroscopic observations allow us to measure effective temperatures, surface gravity values (and therefore stellar masses), and atmospheric chemical compositions. From these studies over many years we know that the great majority of white dwarfs divide into two classes (e.g. McCook & Sion 1999). The DA class have hydrogen atmospheres, and the DB class have *pure* helium atmospheres (no detectable sign of hydrogen and other elements). The DAs account for about 86 per cent of all white dwarfs, while the DBs dominate the rest.

In both of these classes there are objects that provide further information that is subtly encoded in stellar flux variations. These are the pulsators. The cooler hydrogen atmosphere pulsators (DAV class) were discovered serendipitously in the late 1960s (Landolt 1968), while their hotter helium atmosphere cousins were detected following theoretical predictions and a targeted search (Winget 1981; Winget et al. 1982).

The use of pulsating stars to infer some of their intrinsic properties is called stellar seismology or simply *asteroseismology*. Asteroseismology uses the detected pulsation modes of a star to constrain computer models and thereby measure stellar properties, including otherwise hidden interior physical quantities. This endeavour has been a very productive exercise (e.g. Winget 1998) for white dwarfs, in part due to the relative simplicity of the white dwarf structure, but also due to the potentially rich pulsation mode spectrum that results from the nonradial spheroidal (g-mode) pulsation mechanism. All observed white dwarf pulsations are attributed to buoyancy-driven g modes, as the observed periods (70–1500 s) are inconsistent with the predicted periods of pressure (acoustic) waves in the extremely dense white dwarf material: such pulsations would have periods several orders of magnitude smaller, and have never been observed in spite of a number of searches (Robinson 1984; Kawaler et al. 1994; Silvotti et al. 2007).

The more the pulsation modes are identified, the more successful is the white dwarf asteroseismology: in effect, each detected pulsation mode adds another constraint to the modelling process.

Given that the DA objects form a substantial majority of all white dwarfs, it is natural that the DAVs dominate the known objects for these compact pulsators. In fact, following a recent large increase in the detected number of faint white dwarfs (Kleinman et al. 2004), and follow-up programmes to detect more pulsators in these new objects (Mukadam et al. 2004; Kepler et al. 2005a; Castanheira et al. 2006; Mullally et al. 2006), the number of hydrogen atmosphere pulsators has mushroomed to more than 140.

The helium atmosphere DBV pulsators are far fewer: in 2007 there are 17 known objects in this class (Beauchamp et al. 1999; Handler 2001; Nitta et al. 2005, 2007). The southern object EC 20058−5234 (QU Tel, henceforth simply EC 20058) was the eighth DBV to be discovered. It has a B magnitude of approximately 15 and was discovered by the Edinburgh-Cape (EC) faint blue object survey (Stobie et al. 1997). Koen et al. (1995) first reported a study of its properties: they spectroscopically established its DB classification and also demonstrated its variability using the techniques of time-series photometry. Their 20 h of photometry over a four month period in 1994 revealed a total of eight pulsation frequencies and showed that the object was a low-amplitude DBV variable that appeared to be quite stable; this is in complete contrast (on both counts) to the class prototype, GD 358. In fact GD 358 is a large amplitude variable which also exhibits considerable changes in its observed pulsation spectrum over various time-scales ranging from days to years (Kepler et al. 2003).

The Fourier analysis of the discovery data set suggested the presence of low level frequencies below the chosen significance level, so one of us (DOD) proposed a Whole Earth Telescope (WET) campaign (Nather et al. 1990) to probe for coherent periodicities at lower amplitudes than those detected by Koen et al.. Consequently, a WET run was scheduled for dark time in 1997 July, corresponding to the optimal observing season for the target. Following the WET run, regular single-site monitoring has been carried out at primarly Mt John Observatory (NZ).

2 OBSERVATIONS

2.1 WET 1997 photometry

Observing time covering a period of 9 d on four southern telescopes was obtained in 1997 July in order to monitor EC 20058. Time-series aperture photometry was carried out using photometers equipped with blue sensitive photomultiplier tubes and no filters in the light beam at all four observing sites. Consequently, the resulting 'white light' passbands employed in the observations had effective wavelengths similar to that of Johnson B, but with a significantly wider passband.

All photometers used 10-s integration times and operated with essentially 100 per cent duty cycles, given the nature of the photon counting systems employed. The 1.0-m telescope at the South African Astronomical Observatory (SAAO) used a single-channel photometer in combination with autoguiding; both the 1.0-m telescope at Mt John University Observatory (MJUO) in New Zealand and the 1.6-m Itajuba telescope in Brazil were equipped with two-channel photometers; and a three-channel photometer (Kleinman, Nather & Phillips 1996) was used in combination with the CTIO 1.5-m telescope in Chile. A journal of all the observations is provided in Table 1.

Downloaded from https://academic.oup.com/mnras/article/387/1/137/998283 by guest on 15 December 2020

Table 1. Journal of observations of time-series photometry of EC 20058−5234 obtained during the Whole Earth Telescope (WET) extended coverage campaign (XCOV15) in 1997 July. Column 2 provides the observatory and telescope for each run, which are: CTIO = Cerro Tololo Interamerican Observatory, La Serena, Chile (observer: A. Nitta); MJUO = Mount John University Observatory, Lake Tekapo, New Zealand (observer: D. J. Sullivan); OPD = Observatorio Pico dos Dias, Itajubá, Brazil (observer A. Kanaan) and SAAO = South African Astronomical Observatory, Sutherland, South Africa (observers: D. Kilkenny, F. van Wyk). Columns 3 and 4 provide the UT starting date and time for each run, column 5 gives the total number of 10-s integrations in each run, column 6 gives the run length in hours, while the last column is the Barycentric Julian start Date ($BJD^- = BJD - 245\,0000$, see text) for each run corresponding to the UT start times. Note that the two OPD runs marked with an asterisk in column 1 (ra411 and ra413) were not used in the final analysis due to an unexplained timing error (see text).

Run name	Telescope	Date (1997)	UT start	N	ΔT (h)	BJD^- start
dmk057	SAAO 1.0 m	July 2	20:05:27	2745	7.63	632.342 7230
dmk060	SAAO 1.0 m	July 3	19:50:34	2762	7.67	633.332 4031
ra404	OPD 1.6 m	July 4	2:28:00	448	1.24	633.608 4026
jl0497q1	MJUO 1.0 m	July 4	7:30:00	402	1.12	633.818 1279
jl0497q2	MJUO 1.0 m	July 4	8:57:30	2687	7.46	633.878 8927
jl0497q3	MJUO 1.0 m	July 4	16:56:00	591	1.64	634.211 1891
dmk061	SAAO 1.0 m	July 4	20:16:08	384	1.07	634.350 1725
dmk062	SAAO 1.0 m	July 4	22:07:39	1202	3.34	634.427 6157
dmk063	SAAO 1.0 m	July 5	1:42:07	436	1.21	634.576 5529
dmk064	SAAO 1.0 m	July 5	3:00:50	352	0.98	634.631 2180
ra407	SAAO 1.0 m	July 5	5:33:10	996	2.77	634.737 0064
jl0597q1	MJUO 1.0 m	July 5	7:26:30	1394	3.87	634.815 7112
jl0597q2	MJUO 1.0 m	July 5	11:39:00	1112	3.09	634.991 0607
jl0597q3	MJUO 1.0 m	July 5	14:57:00	684	1.90	634.128 5624
jl0597q4	MJUO 1.0 m	July 5	17:04:20	402	1.12	634.216 9895
jl0597q5	MJUO 1.0 m	July 5	18:18:00	160	0.44	634.268 1475
dmk066	SAAO 1.0 m	July 5	19:57:00	2834	7.87	635.336 8984
an-0067	CTIO 1.5 m	July 6	2:43:00	2579	7.16	635.618 8463
jl0697q1	MJUO 1.0 m	July 6	7:31:50	3148	8.74	635.819 4274
jl0697q2	MJUO 1.0 m	July 6	16:50:40	656	1.82	636.207 5105
dmk069	SAAO 1.0 m	July 6	19:28:06	2994	8.32	636.316 8405
ra410	OPD 1.6 m	July 7	0:28:40	1913	5.31	636.525 5696
jl0797q1	MJUO 1.0 m	July 7	7:16:30	2211	6.14	636.808 7902
jl0797q2	MJUO 1.0 m	July 7	13:46:00	782	2.17	636.079 2790
jl0797q3	MJUO 1.0 m	July 7	16:08:00	809	2.25	636.177 8911
dmk071	SAAO 1.0 m	July 7	19:25:06	2956	8.21	637.314 7674
ra411 (∗)	OPD 1.6 m	July 8	4:24:20	1181	3.28	637.689 2385
jl0897q1	MJUO 1.0 m	July 8	11:03:50	291	0.81	637.966 6716
fvw094	SAAO 1.0 m	July 8	20:44:00	312	0.87	638.369 5685
fvw095	SAAO 1.0 m	July 8	23:31:50	1567	4.35	638.486 1204
ra413 (∗)	OPD 1.6 m	July 9	1:35:20	1389	3.86	638.571 8849
fvw097	SAAO 1.0 m	July 9	19:09:00	3033	8.43	639.303 6033
fvw099	SAAO 1.0 m	July 10	19:09:10	3045	8.46	640.303 7252

Good weather at both SAAO and Mt John, combined with poor conditions at CTIO, meant that the bulk of the observations were obtained at just two observatories. However, in spite of the participation of only four telescope sites overall, the WET campaign achieved an observing duty cycle of 64 per cent for the whole 8.3 d observing period, and a duty cycle of 89 per cent for the central 4.4 d when all telescopes contributed. The WET campaign complete coverage can be gleaned from Fig. 1, where the reduced photometry has been graphed in successive 24-h segments.

2.2 Mt John 2004 photometry

Since the 1997 WET campaign, EC 20058 has been regularly monitored from Mt John during its extended southern observing season by one of us (D. J. Sullivan), and some preliminary reports on this work have already appeared (Sullivan & Sullivan 2000; Sullivan 2003). Quality time-series photometry obtained in 2004 June provided confirmation of a pulsation mode that is close to marginal in the WET data set, so it is germane to include some analysis of these data here.

The Mt John 1.0-m telescope in combination with a three-channel photometer (Kleinman et al. 1996) using unfiltered 'white light' (and hence a passband similar to that mentioned previously) was used to acquire time-series photometry of EC 20058 in 2004 June. This photometer includes the functionality of the one used at CTIO in the 1997 WET run, which enables the observer to monitor three regions of the sky using nominally identical miniature blue sensitive (Hamamatsu R647−04) photomultiplier tubes. But, it also incorporates a very useful improvement (e.g. Sullivan 2000). In addition to continuously monitoring the target star, a comparison star and sky background, the comparison star can also function as a continuous guide star. This is achieved by using a dichroic filter in the comparison star's optical train so that the red component of its spectrum is transmitted to a small CCD and the remaining blue component is reflected to the photomultiplier tube. Continuous remote guiding or autoguiding is then possible using only the capabilities of the photometer.

All of the 2004 Mt John photometry was obtained using the three channel photometer operated in autoguiding mode. A good run of clear weather in June led to a 24 per cent duty cycle out of a total observing period of 7.2 d. The results of this work are summarized in Table 2.

3 DATA REDUCTION

We wish to identify periodicities in the light curve that result from stellar pulsation. The first stage in this process is to convert the time-series data to a form that emphasizes the intrinsic stellar intensity changes: this requires the removal of a number of artefacts that result from the observing process. These reductions steps are relatively straight forward (e.g. Nather et al. 1990; Kepler 1993), but in the interests of completeness, and also because we have employed a novel smoothing procedure, we will briefly summarize our steps here.

The EC 20058 field of view has two *faint* companions separated from the target by 2 and 4 arcsec, respectively. For the aperture photometry employed in the work presented here, it was impractical to attempt to separate the target stars from its two companions (especially in indifferent seeing conditions), so all observers used aperture sizes large enough to include all three stars and prevent any errors introduced by imperfect tracking. It is relevant to note at this point that the light curve pulsation amplitudes presented later have not been corrected for this companion star contamination, which has been estimated by Koen et al. (1995) to require multiplication by a factor of ∼1.4.

For each light curve, the sky background (approaching 50 per cent in some cases) for each integration was estimated and then subtracted point by point from the raw light curves. For both the single-channel and two-channel photometers, sky measurements were made by moving the telescope to a blank section of sky at the beginning and end of each run, as well as several times per hour. A sky background time-series curve was constructed for each light

Downloaded from https://academic.oup.com/mnras/article/387/1/137/998283 by guest on 15 December 2020

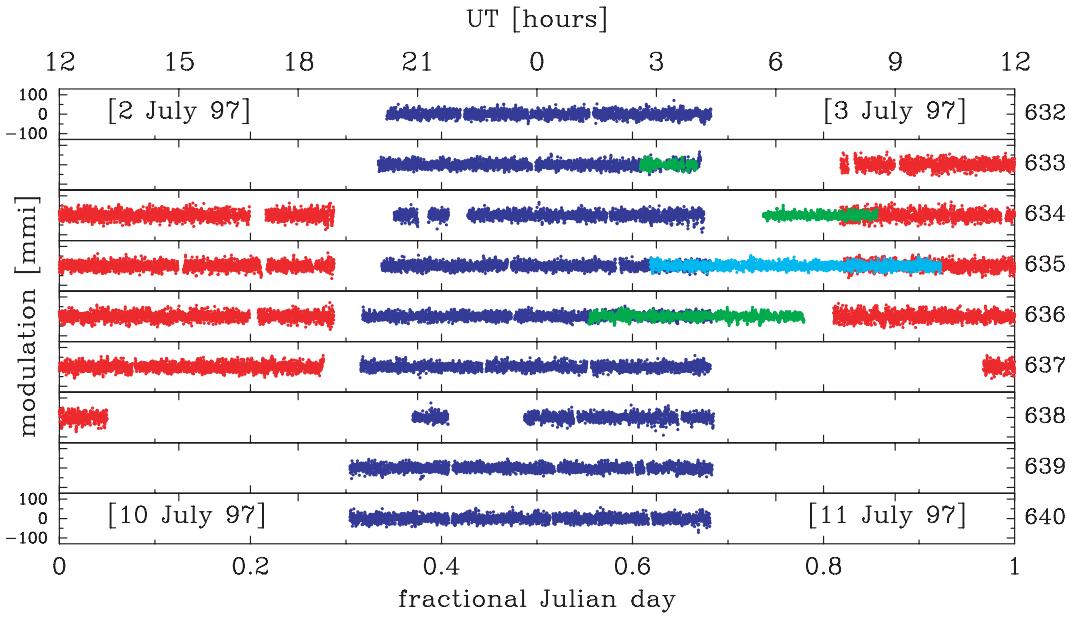

Figure 1. The reduced XCOV15 time-series photometry showing the data quality and the extended coverage provided by the multisite campaign. Each panel represents a whole Julian Day with the actual day determined by adding 245 0000 to the number on the right-hand side of each panel. The vertical axes are in units of millimodulation intensity (mmi) whereby 10 mmi corresponds to a 1 per cent flux variation from the local mean value. The (blue) values in each panel centred around 0 h UT represent SAAO data, the (red) values centred around 12 h UT represent MJUO data, while the CTIO data (light blue) is centred around 6 h UT in the fourth panel from the top and the OPD data (green) segments appear in panels 2, 3 and 5 in the vicinity of 6 h UT. Note that the two OPD runs ra411 and ra413 have not been included in the plot, as they were not included in the final analysis (see discussion in the text). Also, see the online journal article for a colour version of this figure.

Table 2. Journal of observations of time-series photometry of EC 20058−5234 obtained at Mt John Observatory in 2004 June. Columns 3 and 6 give the UT and (modified) Barycentric Julian Date (BJD$^-$) start times for each run and columns 4 and 5 provide the number of useful 10-s integrations and length of run in hours, respectively.

Run name	Date (2004)	UT start	N	ΔT (h)	BJD$^-$ start
ju0904q1	June 9	13:18:30	827	2.97	3166.059 4447
ju1004q2	June 10	12:15:30	2376	6.63	3167.015 7386
ju1104q2	June 11	9:43:10	399	1.15	3167.909 9916
ju1104q3	June 11	11:06:10	2718	7.57	3167.967 6330
ju1204q2	June 12	9:47:20	2010	5.61	3168.912 9289
ju1204q3	June 12	15:29:10	1228	3.43	3169.150 3234
ju1404q2	June 14	12:19:20	1929	6.13	3171.018 5725
ju1604q2	June 16	9:45:20	3067	8.54	3172.911 7024

curve by using either linear or cubic spline interpolation between the measured sky points and then subtracting this computed curve from the raw light curve.

For the three channel photometers (CTIO in the WET run and all of the 2004 Mt John photometry), the relative channel sensitivities were calibrated by measuring sky values for all three channels at the beginning and end of each run. Appropriately adjusted sky values were then subtracted point by point from the other two raw light curves.

The effects of airmass changes were accounted for by fitting low-order polynomials to the sky-corrected data, and then determining fractional deviations of the data points from the fitted values. Although the impact of airmass changes can be readily modelled using a plane-parallel atmosphere approximation, it is just as effective to use the polynomial fitting method.

Accounting for other light-curve artefacts such as the effect of cloud is more problematical, but can be achieved for the two and three channel photometer data by normalizing the sky-corrected target data to the sky-corrected comparison data for those regions affected by cloud. The effect of thin cirrus cloud on a moonless night up to a reduction amount of about 30 per cent can normally be corrected for. This applies in particular to data acquired with the three channel photometers (such as that obtained at Mt John in 2004) since (i) all three channels employ identical blue-sensitive photomultiplier tubes (Hamamatsu R647−04) and (ii) the dichroic optical element in the comparison channel makes its passband effectively similar to that of the target channel (when viewing the hot white dwarfs), irrespective of the spectral type of the comparison star. However, the overriding criterion employed here is that if a data segment appears irreparably cloud-contaminated then it is not included in the combined data set. The data sets listed in Tables 1 and 2 adhere strictly to this criterion.

Any residual 'long-period' variations in each reduced light curve segment (now expressed as fractional deviations from the local mean) were removed using techniques incorporated in the program TS3FIX,[1] developed by one of us (D. J. Sullivan). This program allows the user to fit cubic splines to the data by marking a displayed plot with points at times and flux values selected by the user. The flux fitting values can be determined either by using a local flux average value, or by direct visual selection. Cubic spline fits to these points are then used to smooth the light curve over the entire data segment time interval.

[1] http://whitedwarf.org/ts3fix.

Downloaded from https://academic.oup.com/mnras/article/387/1/137/998283 by guest on 15 December 2020

Undoubtedly, there is an increased component of subjectivity in this procedure when compared with an alternative more objective technique (such as high-pass filtering in the frequency domain); the latter can be readily replicated by others. One might liken it to 'chi-by-eye' visual fitting of an elementary function to a data set compared to use of a more objective fitting procedure, such as least squares. Still, the power of an experienced observer viewing data presented in suitable graphical form and making informed judgements about the quality should not be underestimated; experience has shown that these smoothing procedures are very useful in removing light-curve artefacts that are clearly not related to the WD pulsations of interest.

However, the procedure is obviously open to 'abuse' and consequential loss (or gain) of signal. An important option, which acts as a safeguard, allows the user to calculate Fourier transforms of both the input and modified data and view a comparison plot in order to monitor directly in the frequency domain the changes that are made in the time domain. The procedures can be easily modified or restarted if one is suspicious of the changes made to the light curve. This program has proved to be very effective in eliminating in the time domain obvious artefacts that are not related to white dwarf pulsation, such as inadequate twilight sky correction, and uncorrected transparency variations due to both airmass changes and cloud.

The resulting corrected light curves are then, of course, blind to periodic variations larger than a certain period limit, but it is preferable to remove extraneous power in the time domain rather than simply rely on signal orthogonality in the Fourier domain to differentiate between the signals of interest and other artefacts. Also, given that the white dwarf pulsations of interest are in the range of about 100 to 1000 s, then if one only makes careful use of the program's capabilities on longer data segments (at least an hour or more), then there is a negligible chance of removing any real signal. Besides, previous work (Breger et al. 1995, 1996) has demonstrated that use of the continuous monitoring time-series photometry reported here is inferior to the more traditional 'three-star' photometry when studying longer period ($\sim$ hour or more) variables, such as the δ Scuti stars.

Finally, the observation *start times* for each observatory significant data set were converted to the uniform Barycentric Julian Day (BJD) time-scale, which corresponds to international time (TAI) in units of days transformed to the centre of mass of the Solar system (Standish 1998; Audoin & Guinot 2001).

It is relevant to note here that individual integration times within each listed data segment were not transformed to the BJD time-scale. This results in a maximum timing discrepancy of about a second (1.2 s for the 7.57 h 2004 Mt John June 11 data), so this omission will have a negligible impact on the Fourier analysis of the 10-s integration time-series data. However, these time-scale changes are taken into account in software we have developed to search for long-term period changes.

4 FOURIER ANALYSIS

The standard way to identify the frequency structure in a reduced light curve when the phase information is not required is to calculate a power spectrum. This is presented for the WET data in Fig. 2 in the form of an amplitude 'periodogram' covering the frequency range from 100 to 10 100 μHz, and in which the vertical axes employ the scale millimodulation amplitude (mma). We have employed an

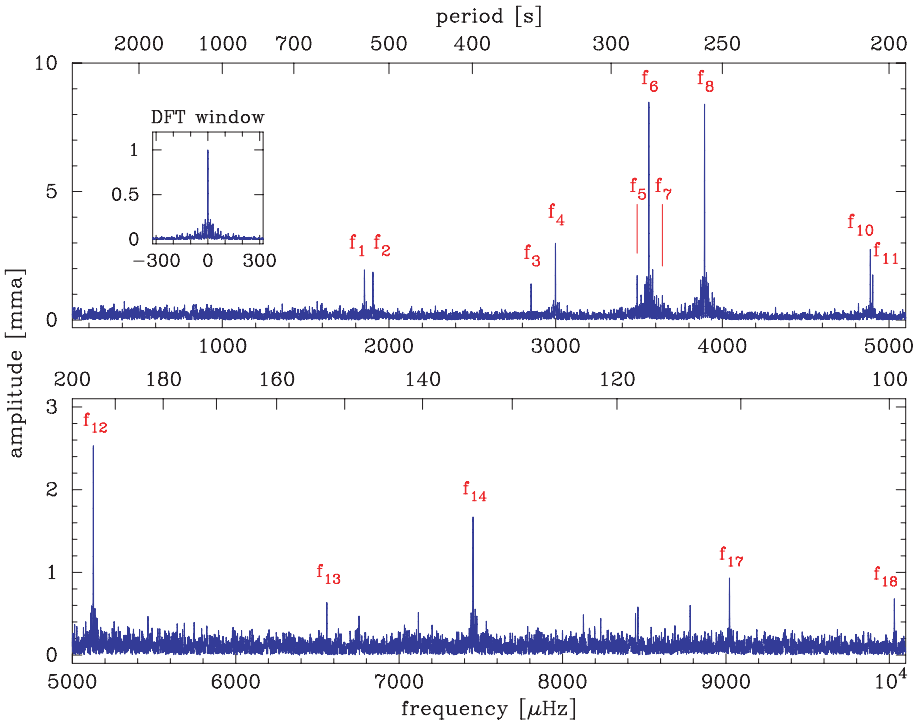

Figure 2. An amplitude periodogram (DFT) of the XCOV15 data set together with the DFT window (plot insert) using the same horizontal scale as the main plots. The vertical axes employ the (linear) unit of mma in which 10 mma corresponds to a 1 per cent amplitude modulation of the light flux. This plot makes clear that the EC 20058 is a multiperiodic low-amplitude pulsator as the two dominant modes have amplitudes less than 10 mma. Readily identifiable periodicities (15 in all) are labelled and there is a suggestion of more real power above 6500 μHz other than the four labelled peaks f_{13}, f_{14}, f_{17} and f_{18}. Note that f_7 is readily identified either by comparing the structure in the DFT at frequencies just above the main f_6 peak with the window function, or (better still) by inspecting a suitably pre-whitened DFT (Fig. 3).

© 2008 The Authors. Journal compilation © 2008 RAS, MNRAS **387,** 137–152

Downloaded from https://academic.oup.com/mnras/article/387/1/137/998283 by guest on 15 December 2020

amplitude scale rather than a power scale (which is now common practice) to represent signal 'power', as this facilitates a more direct intuitive connection with actual sinusoidal variations in the light curve and comparisons with least-squares fitting of sinusoidal functions. Following the work of Scargle (1982), a number of authors use the term 'amplitude periodogram' or simply 'periodogram' for these plots. We will henceforth simply use the acronym DFT (for discrete Fourier transform) to indicate this procedure.

The WET data cover a period of 8.3 d, which corresponds to a frequency resolution of ∼1.4 μHz. The insert panel in Fig. 2 illustrates this resolution by plotting the DFT 'window' for the transform using the same horizontal scale width as the main plot. This window corresponds to the DFT of a synthetic noise-free sinusoid calculated at the same times as all the light curve data: it directly illustrates the frequency resolution *and* the impact of the spurious side lobes, or 'aliases', that result from turning the signal on and off during the observing period. The central plot value has been shifted to zero frequency for clarity. The near continuous WET data have minimal alias interference, which is, of course, the primary reason for the observation strategy pursued by the WET collaboration. Note that in the wider Fourier literature, the additional peaks in a DFT deriving from a particular observing window are termed 'spectral leakage', while the term 'alias' is reserved for effects near the Nyquist frequency resulting from undersampled data. Since we are considering frequencies in our well-sampled data much smaller than the Nyquist frequency (50 000 μHz), following other authors, we will use the term 'alias' for this phenomenon, as it more accurately describes the additional forest of sometimes confusing peaks that occur, particularly for extended data sets with regular daily gaps (e.g. see the right-hand panels in Figs 5 and 6, corresponding to the MJ04 data).

Direct visual inspection of the DFT in Fig. 2 allows one to readily conclude that there are about 15 'real' periodicities present in the data. To this end, the 15 visually obvious frequencies, ranging from ∼2000 to 10^4 μHz, have been labelled f_1 to f_{18} in order in the plot, and also listed in Table 3. At this stage a somewhat conservative (but arbitrary) threshhold has been used to decide that the peaks f_{13} and f_{18}, for example, are real and other smaller amplitude peaks (such as f_9 and others at higher frequencies) are uncertain. Note that the vertical amplitude scales in the upper and lower panels of Fig. 2 are different, and that the reality of f_7 is clear from either a careful comparison of the DFT in the region of f_8 and the form of the window function, or from the analysis presented below.

The EC 20058 light curve is dominated by the beating between the two largest ∼8 mma pulsation modes at 281 and 257 s (f_6 and f_8, respectively). With these modes combining to produce a maximum modulation of less than 2 per cent (∼17 mma) every 50 min, this star is certainly not a large amplitude pulsator. However, as noted previously, the actual intrinsic stellar flux amplitudes are approximately 40 per cent larger due to the uncorrected companion star contamination.

4.1 Light curve pre-whitening

A very useful procedure for separating peaks in the DFT corresponding to real power from those peaks produced by window effects and/or noise is that of 'pre-whitening'. In this procedure, one or more selected frequencies are first removed from the light curve by subtracting least-squares fitted sinusoids, and then a DFT of the 'pre-whitened' light curve is computed. This method is particularly enlightening when one is attempting to identify small amplitude periods that are mixed in with the alias peaks of a much larger amplitude periodicity. As pointed out by Scargle (1982), least-squares fitting of sinusoids in the time domain and computing DFTs are essentially identical analytical procedures, so they both should independently lead to the same conclusions. Consequently, a careful comparison of the window function with the DFT spectrum in the vicinity of a peak should provide the same information as that revealed by the pre-whitening procedure. However, uncertainties in the plots sometimes dominate such comparisons, and therefore the pre-whitening method is often more decisive, as some examples below make clear.

Table 3. Detected frequencies in the DFTs for three EC 20058 data sets. The amplitudes (in millimodulation units) for the 1997 XCOV15 WET run are given in column 5, while the corresponding values for the 2004 Mt John data and the SAAO 1994 discovery data are given in columns 6 and 4, respectively. The adopted combination frequencies are listed in the last column and amplitude values below the relevant significant levels are given in parentheses. Note that the amplitude values have not been adjusted to account for the companion field star light contamination and the 1994 values have been obtained from a subset of the Koen et al. (1995) data – four runs in 1994 July.

Item	Frequency (μHz)	Period (s)	Amplitude (mma) 1994	1997	2004	Combination frequencies
f_1	1852.6	539.8		2.0		
f_2	1903.5	525.4		1.9	1.5	
f_3	2852.4	350.6	(1.6)	1.4	1.3	
f_4	2998.7	333.5	2.2	3.0	2.6	
f_5	3489.0	286.6		1.7	1.3	
f_6	3559.0	281.0	8.8	8.5	7.6	
f_7	3640.1	274.7		1.0		
f_8	3893.2	256.9	8.0	8.4	7.4	
a	3924.2	254.8		(0.5)		
f_9	4816.8	207.6		0.7		
f_{10}	4887.8	204.6	4.2	2.7	2.4	
f_{11}	4902.2	204.0		1.7	1.4	f_2+f_4
f_{12}	5128.6	195.0	3.5	2.5	1.8	
b	5462.5	183.1		(0.5)		f_2+f_6
c	5745.8	174.0		(0.3)		f_1+f_8
f_{13}	6557.6	152.5		0.6		f_4+f_6
d	6745.6	148.2		(0.5)		f_3+f_8
e	7118.0	140.5		(0.5)		$2f_6$
f_{14}	7452.2	134.2	2.3	1.7	2.0	f_6+f_8
f	7533.5	132.7		(0.4)		f_7+f_8
g	8127.3	123.0		(0.5)		f_4+f_{12}
h	8446.8	118.4		(0.5)		f_6+f_{10}
f_{15}	8461.2	118.2		0.6		$f_2+f_4+f_6$
f_{16}	8781.0	113.9		0.6		f_8+f_{10}
f_{17}	9021.7	110.8	1.6	0.9	(1.1)	f_8+f_{12}
f_{18}	10 030.7	99.7		0.7		$f_2+f_4+f_{12}$

Fig. 3 shows the WET DFT covering the same frequency range as for Fig. 2, but with the light curve first pre-whitened by the 10 highest amplitude frequencies: f_1–f_4, f_6, f_8, f_{10}–f_{12} and f_{14}. The y-axis scales in this plot have been expanded, and the removed periodicities are indicated by the downward arrows. The pre-whitening was carried out by simultaneously fitting (via least squares) 10 sinusoids to the data using periods obtained from the original DFT. If the periods are kept fixed, linear least-squares fitting can be used, and in practice this is adequate for the well-defined frequencies in the data (especially if accompanied by a limited grid search).

An examination of the Fig. 3 DFT shows that there are two clearly significant peaks (f_5 and f_7) on either side of the main peak (f_6). In addition, there are two peaks in the upper panel (a and f_9) that look as though they could be significant, a collection of nine peaks

Downloaded from https://academic.oup.com/mnras/article/387/1/137/998283 by guest on 15 December 2020

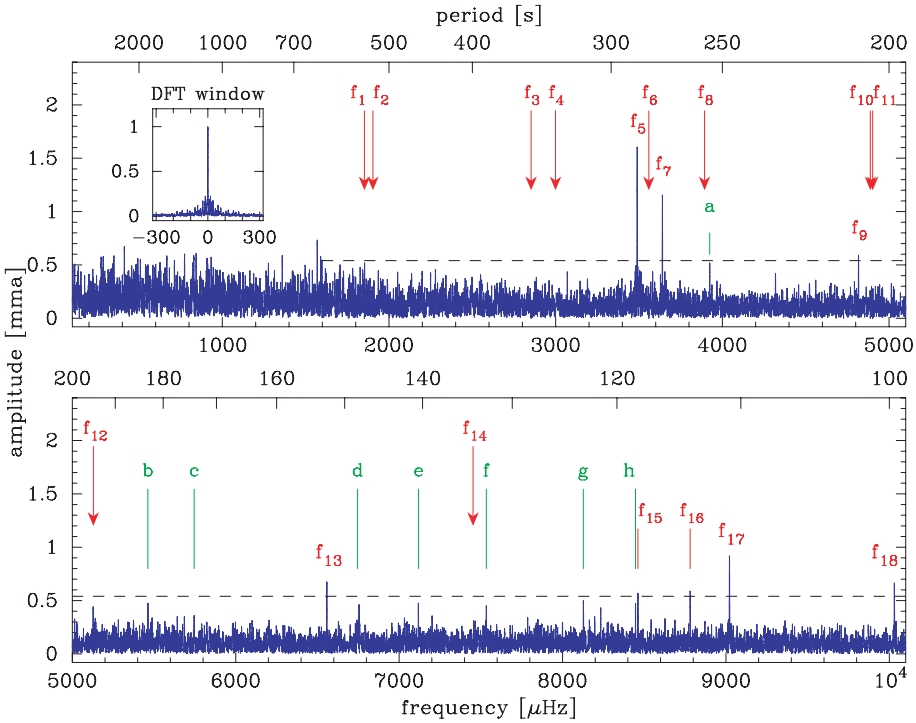

Figure 3. The DFT of the XCOV15 light curve after pre-whitening (see text) by the 10 periodicities with the highest amplitudes: these frequencies are indicated by the downward (red) arrows. The vertical axes use the same units as in plot 2 and the horizontal dashed lines at 0.54 mma in the plots correspond to the 0.001 FAP detection threshhold established by the Monte Carlo data shuffling method discussed in the text. Using this value we can assert that there is real power at ∼4800 μHz (f_9), but not at the frequency just below 4000 μHz marked 'a'. The vertical (green) lines in the lower panel, annotated with the letters 'b–h', correspond to the predicted positions of combination frequencies where there are indications of real power in the DFT (see Table 3). The detected frequencies labelled f_{15} and f_{16} having amplitudes just above the significance threshhold also correspond to the predicted values of combination frequencies.

in the lower panel (labelled b–h, f_{15}, f_{16}), many of whom could be significant, and one or two peaks at low frequencies that need to be investigated. These latter peaks will be discussed in the next section, but clearly we need a quantitative criterion for distinguishing between real and noise peaks.

A detailed inspection of the pre-whitened DFT for the entire data set listed in Table 1 in the vicinity of the dominant periods f_6 and f_8 revealed that there was a small but significant amount of power left in the form of residual 'window mounds' for both frequencies. In other words, the subtraction of the two periodicities from the light curve had not removed all of the power at those frequencies. For a pulsating white dwarf exhibiting very stable and highly coherent luminosity variations, this can be caused by one or more data segments having a timing error. By a process of trial and error, the 'culprits' were determined to be the two OPD observation files ra411 and ra413 marked with an asterisk in Table 1. Upon deletion of these two files from the overall light curve, the pre-whitened DFT produced the results graphed in Fig. 3, and shown in more detail in Fig. 5 (left-hand panels): no signatures of the subtracted frequencies remain. This discovery illustrates the utility of the pre-whitening procedure, as the 'contribution' from the two relatively small data segments could easily have been overlooked otherwise. In order to be certain, the timing discrepancies were investigated graphically by overlaying a time-series plot of the two data segments with the predicted light curve obtained from a least-squares fit of the two dominant frequencies to the rest of the WET data. Both plots clearly revealed the presence of a timing error.

Given the unlikely nature of the alternative hypothesis – the star was behaving differently during these periods – subsequent analysis removed these data from the combined WET light curve. No obvious explanation for the timing error has been found.

4.2 DFT noise simulations

A useful quantitative criterion for differentiating between signal and noise peaks in the DFT is the concept of the false alarm probability (FAP) introduced by Scargle (1982), which makes the statistical nature of the process explicit. Using this concept, one computes the probability of a given peak in the DFT being due to noise for some chosen threshhold. A high threshhold for false positives can be set by ensuring that this probability is small, and only counting peaks that are above this threshhold as real.

Although the FAP can be estimated theoretically on the basis of some assumed model for the noise characteristics (e.g. Scargle 1982), it is preferable and more representative of the actual data to determine it by a Monte Carlo simulation method. And, assisted by the speed of modern computers, this is a practical proposition for even large data sets. Such a simulation has been carried out for the data sets discussed here using the program TSMRAN[2] developed by one of us (D. J. Sullivan). The results of this work for the WET data set are that peaks with an amplitude of 0.54 mma have a FAP value of 0.001, meaning that there is *only* one chance in 1000 that such a peak can be produced by a random noise 'conspiracy'. The corresponding value for the Mt John 2004 (MJ04) data set is 1.2 mma.

[2] http://whitedwarf.org/tsmran.

Downloaded from https://academic.oup.com/mnras/article/387/1/137/998283 by guest on 15 December 2020

These threshholds are marked as horizontal dashed lines in appropriate parts of Figs 3, 5 and 6 showing the pre-whitened DFTs for both data sets.

Although the simulation procedure is conceptually straight forward, there are several points that should be noted and a number of organizational tools are required for a flexible implementation. So, we briefly outline the TSMRAN methodology here.

The essential idea is to start with the reduced light curve that has been pre-whitened by the 'clearly real' frequencies, randomly rearrange the time order of the data points, compute a DFT of these randomized data covering the frequency range of interest, and then record both the maximum (A_m) and the average (A_{av}) value of peak heights in the DFT. Randomizing the time order of the data destroys the coherency of any periodic signal remaining in the light curve but preserves the uncorrelated noise characteristics of the data. The highest peak in the DFT of a time-shuffled data set is then a one sample estimate of the maximum excursion that can occur due simply to random noise effects. If this procedure is repeated a large number of times (say 1000), and the highest peak in each DFT recorded, then one can infer that the maximum value, A_m^{max}, in this ensemble of highest peak values is a direct estimate of the DFT amplitude threshhold for a FAP at the 1 in 1000 level.

It is instructive to plot a histogram of the recorded maximum peaks (A_m) for each DFT: 1000 member ensembles for both the WET and MJ04 data are depicted in Fig. 4. There are two separate such histograms (blue and green) for the WET data centred around 0.4 mma, and one for the MJ04 data centred around 0.9 mma. It is clear that the less comprehensive MJ04 data exhibit larger A_m values, as one would expect.

The program TSMRAN also records the average peak height for each randomized DFT, partly as a check on its operation, and as one might expect there is little variation from DFT to DFT. The histograms of these average peak height values have not been shown, but four times the ensemble average ($4\langle A_{av}\rangle$) for each data set has been indicated in Fig. 4, as one sometimes sees a criterion similar to this used in the literature to identify real power (e.g. Kepler 1993). Note, however, that we are using here (the average of) the average amplitude DFT values and *not* the square root of the average power spectrum values.

A few more comments about the algorithms employed in TSMRAN are relevant. For the relatively large data sets considered here (WET $\sim$ 45k and MJ04 $\sim$ 15k integrations, respectively) a long-period random number generator is required: the routine ran2 from the numerical recipes suite (Press et al. 1992) was found to be equal to the task. One also makes significant efficiency gains by using a fast Fourier transform (FFT) algorithm to compute the DFTs for suitable data sets; the routine realft from Press et al. accomplishes this task in TSMRAN.

However, since FFT algorithms assume that the time-series data correspond to equal contiguous sample intervals, some preliminary organization of the data segments is required before a FFT can be employed. Since all the observations reported in this paper correspond to 10-s integrations it was possible to create an array of integrations that satisfied this attribute (with adequate precision for the intended purpose) without resorting to such (undesirable) procedures as interpolation. All deleted integrations in each 'significant' data segment were restored using zero padding, and the shape of the overall DFT window function was essentially preserved by separately randomizing the points in each segment before combining them together in one overall time-series, all the while maintaining the data gaps using zero padding. Last, the combined time-series is extended to an integer power of two (as required by realft) using zero padding, in order to maximize the efficiency of the FFT procedure.

A comment on the data time-scale is appropriate. Although the above assumption of uniform contiguous integration intervals represents the original terrestrial TAI observation time-scale, offsets are introduced after the transformations to the BJD time-scale. This will have little impact on use of the FFT for the simulation exercise, and negligible impact anyhow if the offsets are not very large. For the record, the total offset change across the WET data is $\sim$7 s, and for the MJ04 data it is $\sim$25 s.

Individual data segments corresponding to each run are read separately into TSMRAN using a list of file names in an input file provided by the user. A glance at Fig. 1 (especially the colour version) shows that there is some data segment overlap (e.g. the fourth panel from the top: SAAO, CTIO and MJUO on July 6). These overlaps were removed by deleting the minimum number of points in order to allow contiguous data to be created.

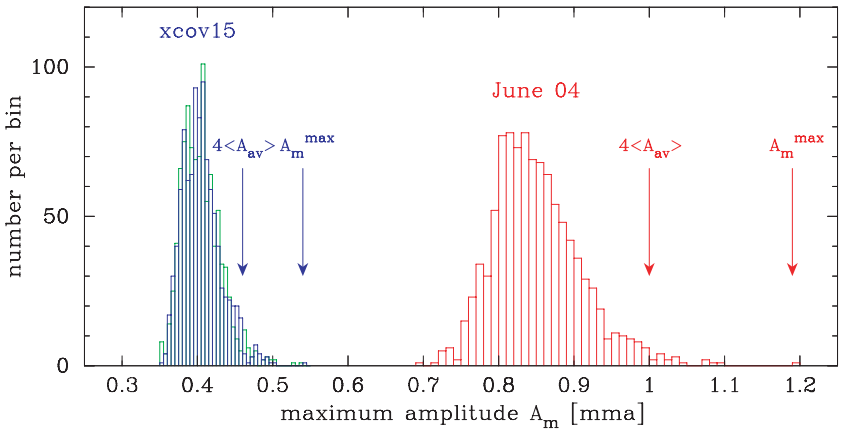

Figure 4. Histograms showing the results of the Monte Carlo data shuffling exercises (see text) invoked to establish a false alarm probability detection threshhold (0.001) for real power in the pre-whitened DFTs. The horizontal axis gives the magnitude of the maximum peak in each DFT of the randomized time-series data and the vertical axis gives the number of occurrences per bin interval. The two histograms (blue and green) centred around 0.4 mma correspond to separate 1000 shuffling trials of the pre-whitened XCOV15 data and use a bin interval of 0.005 mma, while the histogram on the right-hand side employs a bin interval of 0.01 and represents the same process applied to the 2004 multinight Mt John data. For each DFT of the randomized time-series, the maximum peak A_m in the range 1600–10 000 μHz was selected. The downward arrows mark the maximum peaks obtained in all 1000 trials (A_m^{max}) and four times the average DFT peak height (see text) for each ensemble of the DFTs ($4\langle A_{av}\rangle$). See the online journal article for a colour version of this figure.

Downloaded from https://academic.oup.com/mnras/article/387/1/137/998283 by guest on 15 December 2020

A version of the program exists which uses the much slower (computationally inefficient) direct DFT algorithm. This then obviates the need for much of the data organization code in TSMRAN, which admittedly was a significant proportion of the programming coding effort. This method is more general and can be invoked for non-uniform time-series data sets, but it is *significantly* slower. In contrast, the FFT method is extremely fast: on a 'standard' modern laptop the one thousand 64k WET DFTs are computed in less than a minute – effectively 'on the fly', one might say.

At this point it is relevant to emphasize that our simulations are dealing with a random noise model only; other non-random sources of 'noise' (e.g. periodic telescope drive error) need to be handled on a case-by-case basis. In addition, we limited our region of interest to frequencies above 1600 μHz, as (i) there are no obvious peaks in the DFT in this region that stand out above the forest of other peaks and (ii) we would need to consider a higher detection threshhold due to the increasing impact of residual sky noise.

4.3 Detected frequencies

Referring to Figs 2, 3, 5 and 6, and Table 3, we have identified 18 definite frequencies (f_*) in the WET data as being real, using the adopted 0.001 FAP. The amplitudes for these frequencies are given in column 5 of the table, while the amplitudes of other possible frequency detections (a–h) are listed in the table within parentheses.

Two frequencies that merit further discussion are '*a*' and f_9; they are depicted in more detail in the panels of Figs 5 and 6. These frequencies are essentially outside the region where the issue of linear combinations arises (see next section) and their amplitudes are very close to the 0.54 mma significance threshhold. They only first appear as interesting in the pre-whitened DFT of Fig. 3, and the MJ04 data set provides additional information. This is depicted in the right-hand panels of Figs 5 and 6 by graphing both the MJ04 DFTs and pre-whitened DFTs covering the same frequency ranges as for the WET DFTs.

The XCOV15 case for f_9 is clearly presented in the two left-hand panels of Fig. 6. The top left-hand panel shows the DFT with this frequency marked (along with f_{10} and f_{11}), the lower left-hand panel (blue curve) shows the DFT pre-whitened by f_{10} and f_{11} and power at the f_9 frequency above the 0.54 mma threshhold, and the dark (red) curve shows the DFT further pre-whitened by the f_9 frequency in which the peak has disappeared.

The two right-hand panels in Fig. 6 present the MJ04 data case in the same format as the left-hand panels. There is clearly evidence of power in these data at the frequency corresponding to f_9 which follows the shape of the window function and whose maximum peak height is not far below the relevant 1.2 mma significance threshhold. Also, the further pre-whitening procedure removes these peaks from the DFT (red curve). Although the principal peak is below the 1.2 mma MJ04 data significance threshhold, so in isolation would not be interpreted as a detection using our stated threshhold, it does provide definite supporting evidence for the XCOV15 detection.

On the other hand, the case for (and against) '*a*' is presented in a similar manner in Fig. 5. In the lower left-hand panel, the blue curve depicts the XCOV15 data pre-whitened by the two dominant frequencies (f_6 and f_8) and the expanded amplitude scale clearly shows the reality of f_5 and f_7, and also a possibly real frequency '*a*', tantalizingly just below the 0.54 mma significance level. The dark (red) curve is a DFT further pre-whitened by these three frequencies and emphasizes the point that the '*a*' peak could represent real power. However, the same procedure for the MJ04 data tells a different story. The blue curve in the lower right-hand panel shows

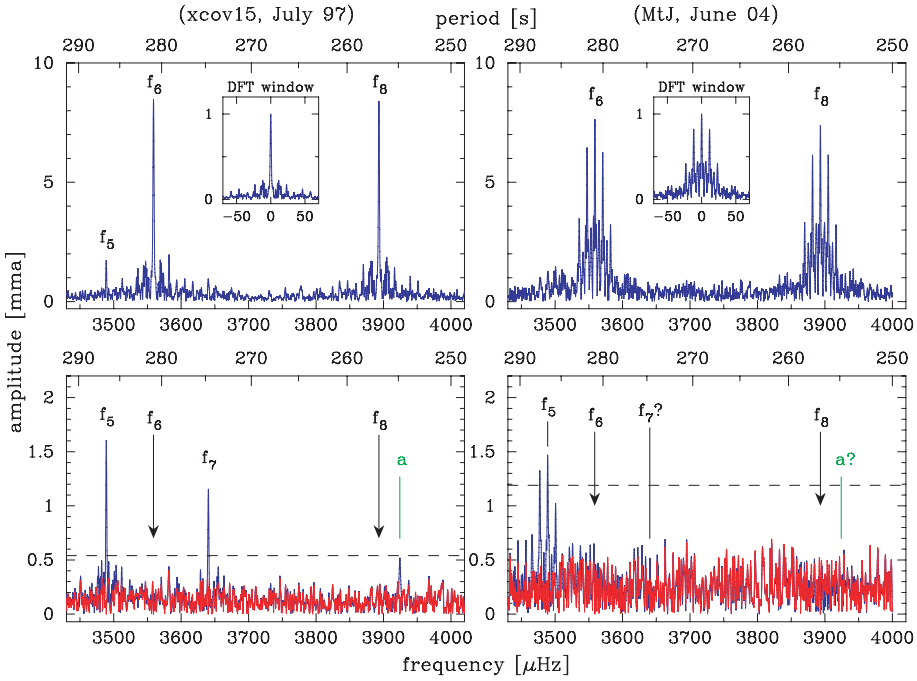

Figure 5. Expanded amplitude DFTs of the frequency region near modes f_6 and f_8, comparing the 1997 XCOV15 data set (top left-hand panel) with the June 2004 (Mt John) data set (top right-hand panel). The panels at the bottom, using an expanded amplitude scale, depict the corresponding DFTs of each time-series pre-whitened by the frequencies f_6 and f_8 (blue curves). The periodicities corresponding to f_5 and f_7 are clearly evident in the pre-whitened XCOV15 data (bottom left-hand panel) but only f_5 is evident in the Mt John data. There is a suggestion of power (marked 'a') in the XCOV15 data adjacent to f_8 that is just below the adopted detection threshhold (dashed line). Both bottom panels also include overlay plots (in red) of pre-whitened DFTs in which the remaining periodicties have been removed. See the online journal article for a colour version of this figure.

Downloaded from https://academic.oup.com/mnras/article/387/1/137/998283 by guest on 15 December 2020

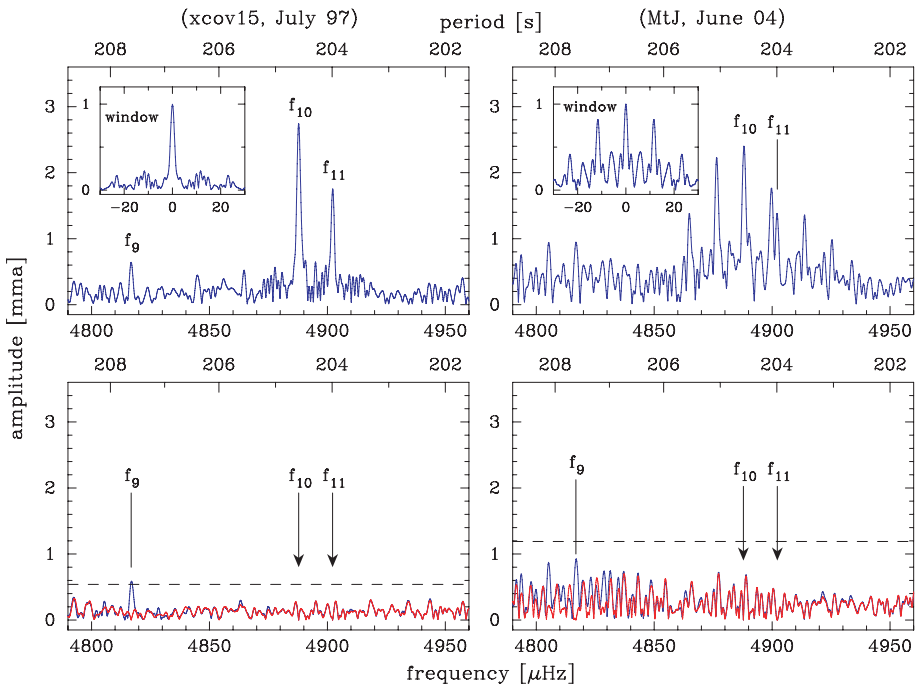

Figure 6. Expanded amplitude DFTs of the frequency region near modes f_{10} and f_{11}, comparing the 1997 XCOV15 data set (top left-hand panel) with the June 2004 (Mt John) data set (top right-hand panel). The panels at the bottom depict the corresponding DFTs (blue curves) of each time-series pre-whitened by the frequencies f_{10} and f_{11}. The horizontal dashed lines in the bottom panels represent the detection threshholds for significant power in the respective data sets (see discussion in Section 4.3). The f_9 frequency is above the detection threshhold in the WET data and, although it is below the Mt John data detection threshhold, it does appear to make its presence felt. The red overlay plots in both bottom panels represent DFTs of each data set further pre-whitened by the f_9 periodicity. See the online journal article for a colour version of this figure.

the MJ04 DFT pre-whitened by the dominant f_6 and f_8 periodicities and there is no evidence of '*a*'.

It is interesting that there is also no evidence for f_7 in the MJ04 data. However, there is without question power at this frequency in the WET data so further confirmation is not required. It does illustrate, though, that power in this quite stable pulsator at various frequencies is still variable at a low level, the result of real physical amplitude instabilities, or perhaps beating.

In view of the above, we have included f_9 as a real detected periodicity, but not included '*a*' – we leave it in the summary table as a bracketed 'may be'.

4.4 Linear combination frequencies

Since the mechanism that converts mechanical movement of stellar material to luminosity variations at the surface appears to be non-linear, both harmonics and combinations of the basic mode frequencies can be expected to appear in the light curve. At least, this is the conclusion of many previous studies of the pulsating white dwarfs – especially the large amplitude pulsators, such as DBV GD 358 (Kepler et al. 2003).

The last column in Table 3 lists whether any of the detected frequencies in the light curve can be identified as a linear combination of other detected frequencies, as well as identifying whether possible linear combinations could account for 'suspiciously' large peaks that are below the 0.54 mma detection threshhold; all these quantities are also indicated on the plot in Fig. 3.

So, all of the actual seven detected frequencies f_{11} and f_{13}–f_{18} can be explained as combination frequencies. This interpretation leaves f_{12} as the highest frequency pulsation mode.

The two largest combination frequencies with amplitudes ∼1.7 mma merit further discussion. The frequency f_{14}, being simply the sum frequency of the two highest amplitude modes (f_6 and f_8) is obviously the first combination to look for, but f_{11} being considered a combination of the lower amplitude modes f_2 (1.9 mma) and f_4 (3.0 mma) is perhaps surprising. Furthermore, these two modes appear to combine separately with f_6 and f_{12} to produce signal power at f_{15} and f_{18}, respectively.

Whereas some of the higher frequency combinations would be difficult to explain as direct mode frequencies using realistic white dwarf models, this is not true for the frequency f_{11}: it is not absolutely certain that this frequency results from non-linear combination effects. However, given the frequency matches mentioned above, and the likely difficulty of explaining the presence of the four closely spaced frequencies f_9–f_{12} in terms of low-order ℓ pulsation modes (see Fig. 7 and discussion next section), we adopt the conservative approach and delete f_{11} from the list of inferred modes.

Column 5 in Table 3 lists the 11 frequencies (f_1–f_{10} and f_{12}) that we consider represent pulsation modes from the work presented here, while columns 4 and 6 in the same table list for comparison all the frequencies detected in the work of Koen et al. (1995) and independently in the MJ04 data set, respectively.

5 COMPARISON WITH MODELS

Our aim here is to compare the 11 detected pulsation modes for EC 20058 with predictions from white dwarf models in order to tell us something about the star. There are two basic approaches to this task. In the first instance we can look for relatively simple systematic trends in the observed pulsation spectrum that depend on

Downloaded from https://academic.oup.com/mnras/article/387/1/137/998283 by guest on 15 December 2020

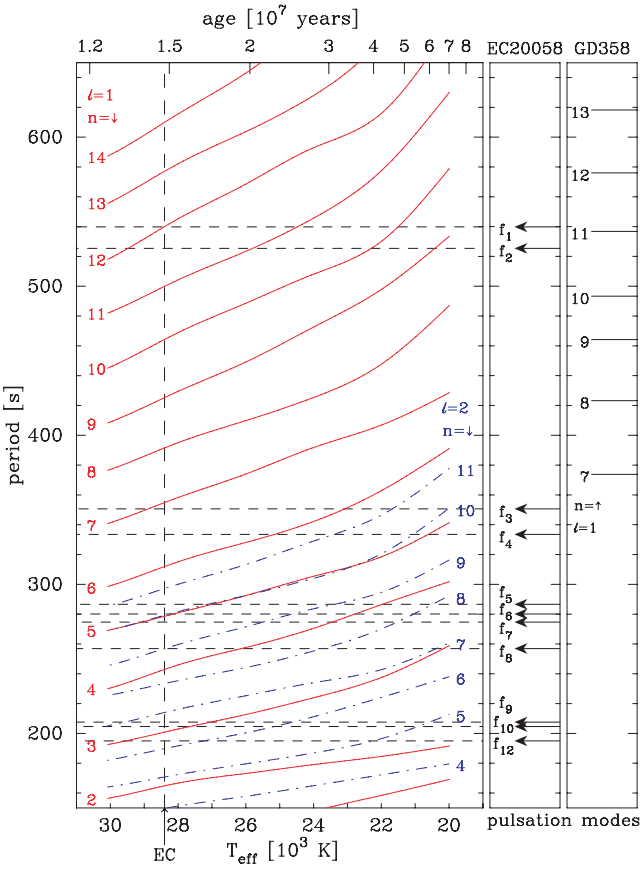

Figure 7. A pulsation mode diagnostic diagram showing the predicted periods of the pulsation modes as a function of effective temperature for a range of 0.6 $M_\odot$ white dwarf models. The left-hand panel graphs all $\ell = 1$ modes (red solid lines) in the period range and only some of the $\ell = 2$ modes (blue dash–dotted lines). The middle panel shows the detected modes for EC 20058 and the right-hand panel shows the modes detected for GD 358 for comparison purposes. See text for more details and the online journal article for a colour version of this figure.

stellar properties. There are, in fact, two of these: one is a sequence of periods with approximately equal spacing (which is obviously best viewed in period space), while the other is 'mode-splitting', which is seen more clearly in frequency space. Secondly, we can adopt a global fitting procedure which endeavours to match the predicted modes to the data, such as that pioneered by Metcalfe, Nather & Winget (2000).

We need two basic results from the relevant pulsation theory in order to look for any systematic trends. The buoyancy-driven g-mode pulsations in white dwarfs (e.g. Unno et al. 1989; Hansen, Kawaler & Trimble 2004) can be characterized by three integer quantum indices: n (or sometimes k), ℓ and m. These indices specify a unique eigenmode of oscillation in which n determines the radial form of the eigenfunction and ℓ and m specify the angular behaviour via a spherical harmonic function $Y_{\ell m}(\theta, \phi)$. If spherical symmetry holds (no rotation and/or magnetic field), then the mode periods, $\Pi_{n\ell}$, are independent of the index m and in the limit of large n we can write

$$\Pi_{n\ell} \approx \Pi_0 \frac{n+\epsilon}{\sqrt{\ell(\ell+1)}} \quad \Longrightarrow \quad \langle \Delta\Pi_\ell \rangle \approx \frac{\Pi_0}{\sqrt{\ell(\ell+1)}}.$$

The quantity Π_0 is inversely proportional to an integral of the Brunt–Väisälä(or buoyancy) frequency over the star profile, and hence decreases with increasing stellar mass (due to increasing local gravitational field strengths). Hence, Π_0 establishes a basic time-scale for the period structure; ϵ can be neglected for our purposes.

Rotation of the star removes the m-degeneracy of the mode frequencies, and to *first order* leads to mode frequencies that are a function of all three quantum indices in the form

$$\nu_{n\ell m} = \nu_{n\ell} + m(1 - C_{n\ell})\Omega,$$

where $\nu_{n\ell}$ is the degenerate frequency, m takes the $2\ell + 1$ integer values between $-\ell$ and $+\ell$, Ω is the rotation frequency of the star and $C_{n\ell}$ takes the approximate dimensionless form $C_{n\ell} = 1/\ell(\ell + 1)$ for high radial overtone modes. The net effect of this is that all (n, ℓ) g-mode pulsations undergo a 'Zeeman-like' splitting due to the rotation of the star which can theoretically be seen as $2\ell+1$ closely spaced frequencies (see Cox 1984, for a nice physical explanation).

A magnetic field also destroys the spherical symmetry and leads to frequency splitting: in the case of a small magnetic field aligned with the pulsation axis, $\ell + 1$ splitting occurs (Jones et al. 1989). Whether any of these modes are sufficiently excited such that they are detectable is another story.

5.1 Model calculations

In order to provide concrete examples, we have determined a range of pulsation modes for a sequence of WD models with effective temperatures between 30 000 and 20 000 K. The results of our calculations are displayed in Fig. 7 (left-hand panel), along with the detected mode periods for EC 20058 (middle panel) and the DBV class prototype (GD 358, right-hand panel).

The WD models and the respective pulsation frequencies were calculated using code that has itself evolved over the years, and is described in a succession of PhD theses at the University of Texas, Austin – see Metcalfe et al. (2000) for a brief description and appropriate references. For our fiducial model, we chose a mass of 0.6 $M_\odot$, a 50/50 C/O core and a fractional helium layer mass of 10^{-3}. Six evolved WD models with effective temperatures at 2000-K intervals between 30 000 and 20 000 K were computed, and the pulsation modes determined for each of these. The pulsation modes for models of intermediate temperatures between these values were estimated by fitting cubic splines to all the mode periods as a function of effective temperature and the results are plotted in Fig. 7: all the $\ell = 1$ mode periods are represented by solid (red) lines in the displayed period range, and a few of the shorter period $\ell = 2$ modes are displayed using the (blue) dash–dotted lines. Since we are using these model calculations to aid the phenomenology discussion below, the precise values of the model parameters are unimportant.

A very obvious feature of the pulsation period structure in the WD models is that all mode periods increase with decreasing effective temperature (e.g. Bradley, Winget & Wood 1994), and therefore increasing age. Over human time-scales this effect is very small, but nevertheless the extremely high stability of many white dwarf pulsators means that this effect can be observed (e.g. Kepler et al. 2005b). We will discuss the prospects for EC 20058 in the last section.

We have chosen to discuss only the lowest order $\ell = 1$ and 2 pulsation modes, as we make the usual assumption (Dziembowski 1977) that the effect of geometrical flux cancellation across the observable stellar disc should ensure that modes with larger ℓ values, if excited, contribute little to the observable flux changes. However, at this point it is appropriate to sound a small note of caution by mentioning that there is evidence of a pulsation mode in the DAV pulsator PY Vul (G 185−32) that has an ℓ value of at least 3 and

Downloaded from https://academic.oup.com/mnras/article/387/1/137/998283 by guest on 15 December 2020

possibly 4 (Thompson et al. 2004; Yeates et al. 2005). It is worth noting, though, that this object exhibits an unusual pulsation spectrum.

For the discussion in the next section we will focus on some details of the 28 000-K model, since this is closest to the effective temperature obtained for EC 20058 by Beauchamp et al. (1999), but see also Sullivan et al. (2007). The pulsation modes in Fig. 7 for this model exhibit a mean period spacing of 37.4 s and a range of 33.4–43.0 s for the $\ell = 1$ modes, and a mean value of 20.4 s with a range of 16.6–23.5 s for the $\ell = 2$ modes.

Among other things, these model values demonstrate that the pulsation theory summarized above does only predict *approximately* constant period spacings for a sequence of modes with a given ℓ and varying n. Also, this theory predicts that the ratio of the 'constant' period spacings for sequences of $\ell = 1$ and 2 in the star should equal $\sqrt{2(2+1)}/\sqrt{1(1+1)} = 1.73$. However, this ratio for the mean period spacings in our computed model (covering the period range in Fig. 7) is 37.4/20.4 = 1.83. This is close to the approximate asymptotic theory value, but not identical, as we are in the low-n regime.

5.2 Period and frequency phenomenology

It follows from the previous discussion that in the first instance we should look for a sequence of observed periods with approximately equal spacing in the pulsation spectrum of EC 20058. As is clear from Fig. 7, such a pattern was detected in GD 358 (Winget et al. 1994; Kepler et al. 2003), and they were all readily interpreted as having spherical degree $\ell = 1$ due to the fact they displayed clear triplet (rotational) splitting. This conclusion was possible, in spite of the complicated nature of the GD 358 pulsation behaviour.

No such simple pattern is immediately apparent in the EC 20058 spectrum. Nevertheless, we will attempt to identify any trends. If one assumes that a number of modes in some sequence are not excited above an observable threshhold, then one could consider some of the pairs f_1–f_2 ($\Delta P = 14.4$ s), f_3–f_4 (17.1 s), f_6–f_8 (24.1 s) [or f_7–f_8 (17.8 s)] and f_9–f_{12} (12.6 s) as visible members of such a sequence. But even ignoring the close spacing between the pairs, the interpair spacings do not match any assumed reasonable sequence. Only the two pairs f_3–f_4 and f_7–f_8 show a similar period spacing with a mean value of about 17.5 s. However, the period spacing between these pairs is not even close to being an integral multiple of this mean value. Even if it was, we would then face the task of interpreting the small period spacing in terms of either a sequence of only $\ell = 2$ excited modes and/or an improbably large model mass $\sim 0.8\,M_\odot$ (as period spacing decreases with model mass).

Another possibility is to temporarily put aside the question of the model mass and consider the two pairs f_6–f_8 (24.1 s) and f_1–f_2 (14.4 s) as members of separate $\ell = 1$ and 2 sequences, respectively. The period spacing ratio is then 24.1/14.4 = 1.67, and this is consistent with both the predicted pulsation theory value (1.73) and the actual model estimates given in the previous section. However, in addition to concerns about the implied total model mass, it is hard to argue convincingly that only two pairs of frequencies are clear evidence of the predicted sequence. Also, we have not independently established any ℓ values for the modes, using for example rotational splitting, as was successfully exploited for GD 358.

The most likely scenario is that we are seeing a combination of $\ell = 1$ and 2 excited modes, coupled with possible rotational frequency splitting. An inevitable conclusion is that the two modes with the largest amplitude ($f_6 \sim 281$ s and $f_8 \sim 257$ s) correspond to different ℓ values, presumably $\ell = 1$ and 2 in some order.

We now investigate the possibility of rotational splitting of pulsation modes in the frequency spectrum. A qualitative inspection of Figs 2 and 3 suggests that some of the modes f_5, f_7, f_9 and even the 'not accepted' frequency 'a' might be caused by rotational splitting. Using the Δf (μHz) values $f_6 - f_5 = 70$ μHz, $f_7 - f_6 = 81$ μHz, $a - f_8 = 31$ μHz and $f_{10} - f_9 = 71$ μHz, we find that the first and fourth of these pairs lead to similar splitting values of ∼70 μHz. If these phenomena are due to splitting, and the modes in question ($f_6 \sim 281$ s and $f_{10} \sim 205$ s) have $\ell = 1$, then the white dwarf is rotating with a period of close to 2 h. We are of course assuming that only one non-zero m component is excited to an observable amplitude out of a possible two for each dipole mode. Note that this interpretation also provides further support (if any is needed) for our argument that real power is present at the frequency f_9. A less likely $\ell = 2$ interpretation for both modes would requires only one out of four possible non-zero m value modes in each case to be excited, and would predict a rotation period close to 4 h.

Given the deductions of other white dwarf rotation rates, a ∼2 h period represents a rapidly rotating white dwarf. This rotation rate is certainly not unphysical, so we tentatively put it forward as a possible interpretation, although the evidence is hardly overwhelming. Note that the pre-white dwarf PG 2131+066 has a measured rotation rate of ∼5 h (Kawaler et al. 1995). Interestingly, the issue of measured white dwarf rotation rates is somewhat controversial as large angular momentum losses via some mechanism are required in order to make these measured rates consistent with the known rotation rates of their much larger progenitors.

Before proceeding to the global modelling analysis presented in the next section, we will include the small (1 mma) satellite frequency f_7 in the mode splitting model that we adopt. A glance at Fig. 5, or the schematic version in Fig. 8, reveals that f_5 and f_7 appear to form an asymmetric pair either side of the large amplitude 'parent' mode f_6 (∼281 s) with separations of 70 and 81.3 s, respectively. There are two ways to produce asymmetric splitting: second-order rotation effects and the inclusion of a magnetic field.

Second-order rotation effects (e.g. Chlebowski 1978) have been detected in the pulsation spectrum of the DAV pulsator L 19−2 (O'Donoghue & Warner 1982; Sullivan 1998). The dominant 192-s mode for this pulsator exhibits two low-amplitude satellite modes

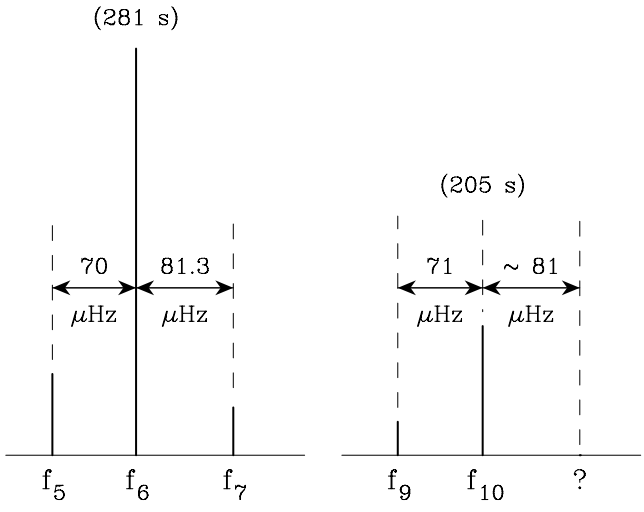

Figure 8. A schematic amplitude spectrum illustrating the proposed rotational and magnetic mode splitting model.

Downloaded from https://academic.oup.com/mnras/article/387/1/137/998283 by guest on 15 December 2020

that are separated by ∼13 μHz from the main peak, and a rotational splitting explanation yields a rotation period of ∼10 h, assuming an $\ell = 1$ value for the mode. Furthermore, the frequency splitting shows a 1 per cent asymmetry, which is consistent with a second-order rotational effect. Even though EC 20058 is estimated to rotate five times faster and the second-order effect depends on the square of the rotation frequency, this is not enough to explain the asymmetry displayed in Fig. 8.

The combined effect of rotation and a magnetic field will also produce asymmetrical splitting. Thus, if the frequency separations adjacent to the f_6 (281-s) mode are divided into a ∼75 μHz symmetrical rotational splitting and a magnetic field frequency shift (increase) of ∼5 μHz, then this would explain the observed triplet. A magnetic field of ∼3 kG and the 2 h rotation period would accomplish this (Winget et al. 1994, appendix). As suggested in Fig. 8, evidence of a similar triplet structure around the f_{10} mode would add considerable weight to this proposal, but as there is no evidence of power at $f_{10} + \sim 81$ μHz, we simply adopt these implied constraints in preparation for the global modelling presented below.

5.3 Model period fitting

Starting with a list of detected pulsation modes and then endeavouring to deduce the parameters of a specific stellar model that reproduces these modes is a classic example of an inversion problem in physics. These tasks are notoriously difficult and are plagued by the lack of unique solutions. However, the apparent relative simplicity of a white dwarf means that a realistic model can be specified by only a few parameters and the potential richness of the g-mode pulsation spectrum provides the possibility of many revealed modes, and hence many constraints to restrict the inversion process.

Following a WET run on the object GD 358 (Winget et al. 1994) that yielded 154 h of near continuous time-series photometry, Bradley & Winget (1994) were able to use the detected pulsation modes to identify a preferred model for this star. They were aided in this task by the fact that the 11 detected normal modes clearly formed a sequence of increasing radial order (n) that were consistent with an $\ell = 1$ assignment, due to the evidence of a triplet structure for each mode. Their asteroseismic analysis enabled a determination of such model parameters as: total mass, surface helium layer mass and effective temperature. Luminosity and a bolometric correction were also estimated, which then led to an asteroseismic distance determination.

A further advance in these modelling procedures has been made more recently by the use of a genetic algorithm to efficiently explore the multidimensional parameter space in a global search for the optimum model or models that fit the pulsation data (Metcalfe et al. 2000). Metcalfe (2003) (and references therein) reports an analysis of GD 358 data that is sensitive to the presumed white dwarf's $^{12}C/^{16}O$ core composition, and thereby yields an indirect measurement of the $^{12}C(\alpha, \gamma)^{16}O$ reaction cross-section at astrophysically relevant energies (as the C/O core composition is determined by the competition between this reaction and the C-forming triple α reaction). Furthermore, Metcalfe et al. (2005) have successfully exploited the global optimization method to analyse pulsation data obtained from dual-site observations (and previous work) of another DBV star CBS 114, and clarify a number of features of its structure.

Note that there has been some controversy concerning these asteroseismic successes, which is related to the fact that both composition variation in the core *and* in the envelope below the helium atmosphere produce similar non uniformities in the period spectrum (Fontaine & Brassard 2002; Brassard & Fontaine 2003; Montgomery, Metcalfe & Winget 2003).

Given that the analysis in the previous subsection did not uncover any clear trends in the pulsation mode data (except for perhaps the rotational and magnetic splitting we have proposed), one would hope that use of a global fitting procedure could yield some definitive results. Adopting this mode splitting model reduces the 11 identified normal modes to only eight independent modes with different n and/or ℓ values. This is comparable to the number of modes available for the analyses of both GD 358 and CBS 114 discussed above. But, in contrast to these other two pulsators where additional constraints are evident ($\ell = 1$ assignments with consecutive radial index values), the EC 20058 pulsation spectrum offers none of these clues. The revealed modes are most likely a mixtures of $\ell = 1$ and 2.

Using the 8-mode data set, we applied a modified version of the global model-fitting procedure originally described by Metcalfe, Montgomery & Kawaler (2003). This version of the code incorporates the OPAL radiative opacities (Iglesias & Rogers 1996) rather than the older LAO data (Huebner et al. 1977), which are known to produce systematic errors in the derived temperatures (Fontaine & Brassard 1994). The fitting procedure uses a parallel genetic algorithm (Metcalfe & Charbonneau 2003) to minimize the rms residuals between the observed and calculated periods (σ_P) for models with effective temperatures ($T_{\rm eff}$) between 20 000 and 30 000 K, and stellar masses ($M_\star$) between 0.45 and 0.70 $M_\odot$. We restricted the mass range more than in earlier applications to avoid a family of models with high masses, which contain such a high density of $\ell = 2$ modes that they can match essentially any set of observed periods. We allowed the base of the uniform He/C envelope to be located at an outer mass fraction $\log (M_{\rm env}/M_\star)$ between −2.0 and −4.0. The base of the pure He surface layer could assume values of $\log(M_{\rm He}/M_\star)$ between −5.0 and −7.0.

Since we have almost no information about the spherical degree of the modes, we assumed only $\ell = 1$ and 2 modes were observable and calculated all of the periods in the range 150–600 s for each model; we then selected the closest model period for each observed mode. This procedure tends to bias the identification in favour of $\ell = 2$ modes since there are always more of them for a given model. Following Metcalfe, Montgomery & Kanaan (2004), we required an $\ell = 2$ mode to be closer to the observed period by a factor $N_{\ell=2}/N_{\ell=1}$ for selection as a better match. In effect, we optimized the mode identification internally for each model evaluation, while the genetic algorithm optimized the values of the other four parameters.

To quantify the effect of our ignorance of the core composition, we repeated this fitting procedure using three different types of cores: pure C, a uniform 50:50 mixture of C/O, and pure O. The results of these three fits are shown in Table 4, and the corresponding model periods and mode identifications are shown in Table 5. With the exception of the period at 350.6 s, the mode identifications are the same for all three fits. The fit using a pure C core identified the 350.6 s period as ($\ell = 1$, $n = 7$) while the other two fits both preferred an

Table 4. Optimal model parameters for EC 20058.

Parameter	C (pure)	C/O 50:50	O (pure)	Average
$T_{\rm eff}(K)$	28 100	28 200	28 400	28 250 ± 150
$M_\star(M_\odot)$	0.550	0.550	0.550	0.550 ± 0.005
$\log(M_{\rm env}/M_\star)$	−3.56	−3.60	−3.62	−3.59 ± 0.03
$\log(M_{\rm He}/M_\star)$	−6.42	−6.46	−6.48	−6.45 ± 0.03
σ_P(s)	1.89	1.94	2.03	–

Downloaded from https://academic.oup.com/mnras/article/387/1/137/998283 by guest on 15 December 2020

Table 5. Periods and mode identification.

$f_{\rm num}$	$P_{\rm obs}$	$P_{\rm calc}$ Pure C	50:50 C/O	Pure O	ℓ	n
f_{12}	195.0	192.57	192.82	192.76	2	6
f_{10}	204.6	205.23	205.72	205.86	1	3
f_8	256.9	260.37	260.61	260.85	2	9
f_6	281.0	280.84	281.08	281.13	1	5
f_4	333.5	330.89	330.65	330.70	2	12
f_3	350.6	350.44	350.44	350.39	2,1	13,7
f_2	525.4	523.98	524.47	524.60	2	21
f_1	539.8	540.92	541.01	541.27	2	22

identification of ($\ell = 2$, $n = 13$). The pure C model also includes this $\ell = 2$ mode, and although it was closer to the observed period than the $\ell = 1$ mode, it was not close enough to overcome the requirement that it be closer by the factor $N_{\ell=2}/N_{\ell=1}$. Thus, the mode identification appears to be reasonably robust.

All three core compositions yield very good fits to the observed periods, with $\sigma_{\rm P} \sim 2$ seconds in all cases. This is slightly better than the quality of the four-parameter fits achieved for the DBV white dwarfs GD 358 and CBS 114 by Metcalfe et al. (2005) using the same code. The main effect of the different core compositions is to modify the optimal value of $T_{\rm eff}$, and to make slight adjustments to the locations of the two near-surface composition gradients. The average values of the mass and effective temperature are in good agreement with the spectroscopically determined values (Beauchamp et al. 1999), the total envelope mass is within the range expected from stellar evolution theory (D'Antona & Mazzitelli 1979), and the thickness of the pure He surface layer, when compared to similar measures for GD 358 and CBS 114, is consistent with the expectations of diffusion theory (Metcalfe 2007).

5.4 Review of the global fitting

At this point it is prudent to pause and critically examine where our analysis has led us. From a total of 11 detected pulsation modes, we assumed that eight of them had independent n and ℓ values, and then our modelling has identified unique index values for all but one of these modes (Table 5). An obvious question is how plausible and unique is our 'best' model?

One interesting result, which was foreshadowed in our previous general discussion, is the assignment of different ℓ values (1 and 2) to the dominant 281 s (f_6) and 257 s (f_8) equal (observed) amplitude modes. Taking into account the expected larger geometrical flux cancellation from an $\ell = 2$ mode, this requires a higher physical amplitude for the 257-s mode to compensate for this geometrical effect. In isolation, a more plausible assumption might be that both modes have the same $\ell = 1$ value, and the small period spacing between them is explained by an unusually high mass ($\sim 0.8\,{\rm M}_{\odot}$) for the star. But, we do have external constraints: model fits to EC 20058's optical spectrum are not consistent with such a high mass (Beauchamp et al. 1999; Sullivan et al. 2007). It is also interesting that a high mass can be ruled out largely through asteroseismic constraints, as discussed in the next paragraph.

As a further check on our conclusions, we undertook a relatively exhaustive exploration of model parameter space using a grid of pre-computed models. Unconstrained fitting to the pulsation spectrum using criteria similar to that discussed previously yielded two competing best fit models: the 'low-mass' ($\sim 0.55\,{\rm M}_{\odot}$) ones discussed previously, and a 'high-mass' family with M $\sim$0.8–0.9 $\rm M_{\odot}$. However, when the 281-s (f_6) mode was constrained to be $\ell = 1$, then the high-mass family did not remain competitive, and hence the best model assigned $\ell = 2$ to the 257-s mode and predicted a mass of $0.55\,{\rm M}_{\odot}$, confirming the above. Assigning $\ell = 1$ to the 281-s mode is not totally arbitrary and is consistent with the rotational and magnetic mode splitting arguments developed in the previous section.

Thus, two independent constraints added to the asteroseismic fitting resulted in the same conclusion. We conclude our modelling discussion at this point, and add the comment that a more exhaustive modelling effort is currently underway.

6 SUMMARY AND FUTURE WORK

The work presented here has significantly extended our knowledge of the helium atmosphere pulsating white dwarf, EC 20058−5234 beyond that revealed by the discovery observations of Koen et al. (1995). Analysis of nearly 135 h of photometric time-series data obtained by four southern telescopes during the 8-d 1997 WET run XCOV15, along with 42 h of single-site data obtained during a week of observing at Mt John Observatory in 2004 June has more than doubled the number of detected frequencies from 8 to 18 (Table 3).

Following a detailed simulation procedure that we undertook, we are confident at the 1 in 1000 FAP level that the power in the detected modes (the lowest 0.6 mma frequencies, in particular) is not simply the result of random noise fluctuations.

Although we were able to identify signal power in our WET data at 18 different frequencies that are above our adopted 0.54 mma significance level (and one possibility just below: '*a*'), only 11 of these could reasonably be viewed as pulsation modes. The seven other periods are readily characterized as combination frequencies resulting from the non-linear processes that translate mechanical movement of the stellar material into observable flux changes.

Our initial investigation of the detected pulsation mode structure revealed no clear systematic trends, except for perhaps a rotational splitting value of 70 (or 75) μHz for two of the modes. Interestingly, the modes suspected of showing rotational splitting were independently identified as the only $\ell = 1$ modes from our objective fitting method, which could explain why they are the only modes that show this behaviour. We (tentatively) interpret this as evidence that the white dwarf is rotating with a period of about 2 h.

A global fitting analysis of the period structure, following procedures similar to those described in Metcalfe et al. (2000), resulted in three models with different core compositions that all yielded very good fits to the eight assumed independent observed periods (see Tables 4 and 5). All models had similar effective temperatures ($\sim$28 200 K) and masses (0.55 $\rm M_{\odot}$) that were in good agreement with the spectroscopically determined values (Beauchamp et al. 1999; Sullivan et al. 2007). This analysis provided no insights on the core composition, as the fits were largely insensitive to the three different chosen C/O ratios. As expected from the earlier discussions, the global fitting assigned different mode ℓ values to the two dominant pulsation frequencies: f_6, $\ell = 1$ and f_8, $\ell = 2$.

Although the number of known DBV objects is relatively small (17), and is totally dwarfed by the current known number of cooler hydrogen atmosphere (DAV) pulsators (now exceeding 140), it is still tempting to draw some conclusions about the nature and extent of the DB instability strip along the lines discussed by Mukadam et al. (2004) (see also Mukadam et al. 2005). Even using just the two stars GD 358 and EC 20058, we can infer that the DBVs mimick the characteristics exhibited by the DAVs. GD 358 has a relatively low

Downloaded from https://academic.oup.com/mnras/article/387/1/137/998283 by guest on 15 December 2020

effective temperature (24 900 K, Beauchamp et al.) and exhibits both large amplitude pulsations and unstable behaviour (modes come and go), while EC 20058 has a significantly higher effective temperature (28 400 K) and displays low-amplitude very stable behaviour. Similar behaviour is found in the ensemble of DAVs, and some authors have divided them into hot (hDAV) and cold (cDAV) pulsators (e.g. Mukadam et al. 2004). The hDAVs feature only a few detectable pulsation modes that have low amplitudes and are relatively stable, while the cDAVs exhibit many variable modes. This is surely telling us something about the onset and cessation of pulsation as the white dwarf cools through the temperature dependent instability strip.

Certainly compared with GD 358, EC 20058 is a stable pulsator in terms of both mode amplitude and period. The two lower panels in Fig. 5, in particular, demonstrate that the mode amplitude stability might be subject to some qualification, as the mode f_7 has an amplitude of 1.2 mma in the WET data, but there is no evidence of it in the MJ04 data. An alternative possibility is that beating between unresolved modes explains the low-level amplitude variability. However, the dominant modes are always present in the photometry with about the same amplitudes.

Both data sets presented here indicate that EC 20058 has *very* stable pulsation periods. This conclusion is also supported by other observational work (Sullivan & Sullivan 2000; Sullivan 2003, 2005). This means that we can attempt to measure evolutionary cooling effects over human time-scales. The key point is that the DBV white dwarf model periods increase with decreasing temperature (e.g. Bradley et al. 1994), so careful monitoring of a stable mode period or periods over a multiyear interval should in principle lead to a detectable period change and therefore a direct measure of the stellar evolutionary time-scale.

As one might expect, the models for both the cooler DAV white dwarfs and the much hotter DOV pulsating pre-white dwarfs also predict period increases with decreasing temperature. More than 10 yr of time-series photometry (including several WET runs) on the DOV object PG 1159−035 produced a measured period increase (Costa, Kepler & Winget 1999), largely because the predicted rate is several orders of magnitude higher than for the DBVs. Note that as a direct testimony on the difficulties of these measurements, a 'false alarm' result was published at an earlier date (Winget et al. 1985, 1991). Kepler and collaborators (Kepler et al. 2005b) have been monitoring the highly stable DAV G 117−B15A over three decades and have finally detected a definite period change. As recently pointed out by Winget et al. (2004), with sufficient quality data one might expect to measure a period change for a DBV over a time-scale as short as ∼5 yr. This is the aim of an ongoing observational campaign featuring EC 20058 (Sullivan 2005).

The cooling mechanism for both the very hot pre-white dwarfs and the hot white dwarfs is dominated by neutrino emission from the high-temperature degenerate cores (e.g. Winget, Hansen & Van Horn 1983; O'Brien & Kawaler 2000; Winget et al. 2004). Models show that this core neutrino flux exceeds the surface photon flux down to an effective temperature of about 25 000 K, depending on the mass of the star.

In fact, Winget et al. (2004) demonstrate that a DB model with a typical mass of $0.6\,M_{\odot}$ with an effective temperature of 28 400 K (the EC 20058 estimated value), has a neutrino cooling flux approximately four times that of the photon flux. These facts suggest a very interesting experiment: measure a period change and compare this rate with two values obtained from models that include and exclude the neutrino mechanism. Then, provided we are confident that the star's mass and effective temperature are in the right-hand region, we have the exciting possibility that we are using a pulsating star to directly test a key low-energy prediction of electroweak theory.

This is the current promise for EC 20058 as at these effective temperatures the evolutionary cooling occurs at approximately constant radius, in contrast to the much hotter pre-white dwarfs (Winget, Hansen & Van Horn 1983). In the latter case, both continuing gravitational contraction and evolutionary cooling have an impact on the pulsation periods so any comparisons with theoretical predictions are less certain.

Given the potential importance of this star, we have recently undertaken both time-series photometry and spectroscopy using one of the Magellan 6.5 m telescopes (Sullivan et al. 2007), in addition to seasonal monitoring using Mt John Observatory (Sullivan 2003).

ACKNOWLEDGMENTS

We thank the various Time Assignment Committees for the award of telescope time, and in particular, DJS would like to thank the Department of Physics and Astronomy at the University of Canterbury for the generous allocation of Mt John observing time for this project. He also thanks Grant Kennedy for help in reducing the MJ04 data set and the VUW Faculty of Science for financial support. We also thank Scot Kleinman for a very thorough reading of initial drafts of the paper. TSM would like to thank Mark Waddoups for his assistance with the model fitting. Finally we thank an anonymous referee for careful reading of the manuscript and constructive comments that led to an improvement in the clarity of the presentation.

REFERENCES

Audoin C., Guinot B., 2001, The Measurement of Time: Time Frequency and the Atomic Clock. Cambridge Univ. Press, Cambridge
Beauchamp A., Wesemael F., Bergeron P., Fontaine G., Saffer R. A., Liebert J., Brassard P., 1999, ApJ, 516, 887
Bradley P. A., Winget D. E., 1994, ApJ, 430, 850
Bradley P. A., Winget D. E., Wood M. A., 1994, ApJ, 406, 661
Brassard P., Fontaine G., 2003, in de Martino D., Silvotti R., Solheim J.-E., Kalytis R., eds, NATO Sci. Ser. Vol. 105, White Dwarfs. Kluwer, Dordrecht, p. 259
Breger M. et al., 1995, A&A, 297, 473
Breger M. et al., 1996, A&A, 309, 197
Castanheira B. G. et al., 2006, A&A, 450, 227
Chlebowski T., 1978, Acta Astron., 28, 441
Costa J. E. S., Kepler S. O., Winget D. E., 1999, ApJ, 522, 973
Cox J. P., 1984, PASP, 582, 577
D'Antona F., Mazzitelli I., 1979, A&A, 74, 161
Dziembowski W. A., 1977, Acta Astron., 27, 203
Fontaine G., Brassard P., 1994, in Chabrier G., Schatzman E., eds, IAU Colloq. 147, The Equation of State in Astrophysics. Cambridge Univ. Press, Cambridge, p. 347
Fontaine G., Brassard P., 2002, ApJ, 581, L33
Handler G., 2001, MNRAS, 323, L43
Hansen C. J., Kawaler S. D., Trimble V., 2004, Stellar Interiors: Physical Principles, Structure and Evolution, 2nd edn. Springer-Verlag, New York
Huebner W. F., Merts A. L., Magee N. H., Argo M. F., 1977, Los Alamos Scientific Laboratory report, LA-6760-M
Iglesias C. A., Rogers F. J., 1996, ApJ, 464, 943
Jones P. W., Pesnell W. D., Hansen C. J., Kawaler S. D., 1989, ApJ, 336, 403
Kawaler S. D., Bond H. E., Sherbert L. E., Watson T. K., 1994, AJ, 107, 298
Kawaler S. D. et al., 1995, ApJ, 450, 350
Kepler S. O., 1993, Balt. Astron., 2, 515
Kepler S. O. et al., 2003, A&A, 401, 639

Downloaded from https://academic.oup.com/mnras/article/387/1/137/998283 by guest on 15 December 2020

Kepler S. O., Castanheira B. G., Saraiva M. F. O., Nitta A., Kleinman S. J., Mullally F., Winget D. E., Eisenstein D. J., 2005a, A&A, 442, 629
Kepler S. O. et al., 2005b, ApJ, 634, 1311
Kleinman S. J., Nather R. E., Phillips T., 1996, PASP, 108, 356
Kleinman S. J. et al., 2004, ApJ, 607, 426
Koen C., O'Donoghue D., Stobie R. S., Kilkenny D., Ashley R., 1995, MNRAS, 277, 913
Landolt A. U., 1968, ApJ, 153, 151
McCook G. P., Sion E. M., 1999, ApJS, 121, 1
Metcalfe T. S., 2003, ApJ, 587, L43
Metcalfe T. S., 2007, Commun. Asteroseismol., 150, 227
Metcalfe T. S., Charbonneau P., 2003, J. Comput. Phys., 185, 176
Metcalfe T. S., Nather R. E., Winget D. E., 2000, ApJ, 545, 974
Metcalfe T. S., Montgomery M. H., Kawaler S. D., 2003, MNRAS, 344, L88
Metcalfe T. S., Montgomery M. H., Kanaan A., 2004, ApJ, 605, L133
Metcalfe T. S., Nather R. E., Watson T. K., Kim S.-L., Park B.-G., Handler G., 2005, A&A, 435, 649
Montgomery M. H., Metcalfe T. S., Winget D. E., 2003, MNRAS, 344, 657
Mukadam A. S. et al., 2004, ApJ, 607, 982
Mukadam A. S., Montgomery M. H., Winget D. E., Kepler S. O., Clemens J. C., 2005, ApJ, 625, 966
Mukadam A. S., Winget D. E., von Hippel T., Montgomery M. H., Kepler S. O., Costa A. F. M., 2004, ApJ, 612, 1052
Mullally S. E., Thompson S. E., Castanheira B. G., Winget D. E., Kepler S. O., Eisenstein D. J., Kleinman S. J., Nitta A., 2006, ApJ, 640, 956
Nather R. E., Winget D. E., Clemens J. C., Hansen C. J., Hine B. P., 1990, ApJ, 361, 309
Nitta A., Kleinman S. J., Krzesinski J. et al., 2005, in Koester D., Moehler S., eds, ASP Conf. Ser. Vol. 334, 14th European Workshop on White Dwarfs. Astron. Soc. Pac., San Francisco, p. 585
Nitta A. et al., 2007, Commun. Asteroseismol., 150, 249
O'Brien M. S., Kawaler S. D., 2000, ApJ, 539, 372
O'Donoghue D. E., Warner B., 1982, MNRAS, 200, 563
Press W. H., Flannery B. P., Teukolsky S. A., Vetterling W. T., 1992, Numerical Recipes, 2nd edn. Cambridge Univ. Press, Cambridge
Robinson E. L., 1984, AJ, 89, 1732
Scargle J. D., 1982, ApJ, 263, 835
Silvotti R., Fontaine G., Pavlov M., Marsh T. R., Dhillon V. S., Littlefair S. P., 2007, in Napiwotzki R., Burleigh M., eds, ASP Conf. Ser. Vol. 372, 15th European Workshop on White Dwarfs. Astron. Soc. Pac., San Francisco, p. 593
Standish E. M., 1998, A&A, 336, 381
Stobie R. S. et al., 1997, MNRAS, 287, 848
Sullivan D. J., 1998, Balt. Astron., 7, 159
Sullivan D. J., 2000, Balt. Astron., 9, 425
Sullivan D. J., 2003, in de Martino D., Silvotti R., Solheim J.-E., Kalytis R., eds, NATO Science Ser. Vol. 105, White Dwarfs. Kluwer, Dordrecht, p. 231
Sullivan D. J., 2005, in Koester D., Moehler S., eds, ASP Conf. Ser. Vol. 334, 14th European Workshop on White Dwarfs. Astron. Soc. Pac., San Francisco, p. 495
Sullivan D. J., Sullivan T., 2000, Balt. Astron., 9, 81
Sullivan D. J., Metcalfe T., O'Donoghue D., Winget D. E. et al., 2007, in Napiwotzki R., Burleigh M., eds, ASP Conf. Ser. Vol. 372, 15th European Workshop on White Dwarfs. Astron. Soc. Pac., San Francisco, p. 629
Thompson E. S., Clemens J. C., van Kerkwijk M. H., O'Brien S., Koester D., 2004, ApJ, 610, 1001
Unno W., Osaki W., Ando H., Saio H., Shibahashi H., 1989, Nonradial Oscillations of Stars, 2nd edn. Univ. Tokyo Press, Tokyo
Winget D. E., 1981, PhD thesis, Univ. Rochester
Winget D. E., 1998, J. Phys.: Condens. Matter, 10, 11247
Winget D. E., Robinson E. L., Nather R. E., Fontaine G., 1982, ApJ, 262, L11
Winget D. E., Hansen C. J., Van Horn H. M., 1983, Nat, 303, 781
Winget D. E., Kepler S. O., Robinson E. L., Nather R. E., O'Donoghue D., 1985, ApJ, 292, 606
Winget D. E. et al., 1991, ApJ, 378, 326
Winget D. E. et al., 1994, ApJ, 430, 839
Winget D. E., Sullivan D. J., Metcalfe T. S., Kawaler S. D., Montgomery M. H., 2004, ApJ, 602, L109
Yeates C. M., Clemens J. C., Thompson S. E., Mullally F., 2005, ApJ, 635, 1239

This paper has been typeset from a TEX/LATEX file prepared by the author.

Downloaded from https://academic.oup.com/mnras/article/387/1/137/998283 by guest on 15 December 2020